IOP Publishing Phys. Med. Biol. 65 (2020) 085010 https://doi.org/10.1088/1361-6560/ab7685

Physics in Medicine & Biology

IPEM Institute of Physics and Engineering in Medicine

PAPER

Meshless reconstruction technique for digital tomosynthesis

Vadim Y Soloviev, Kate L Renforth, Conrad J Dirckx and Stephen G Wells

Adaptix Ltd, Oxford University Begbroke Science Park, Woodstock Road, Oxford OX5 1PF, United Kingdom

E-mail: vadim.soloviev@adaptiximaging.com

Keywords: x-ray tomography, tomosynthesis, image reconstruction

RECEIVED
28 August 2019

REVISED
24 January 2020

ACCEPTED FOR PUBLICATION
14 February 2020

PUBLISHED
20 April 2020

Abstract

A novel meshless reconstruction algorithm for digital tomosynthesis (DT) is presented and assessed against experimental data. The algorithm does not require a three-dimensional grid or mesh allocation and performs a slice-by-slice reconstruction where each slice position can be chosen at runtime. The methodology is based on the filtered backprojection algorithm adapted to DT. However, in the traditional approach the backprojection comes first and the filtering follows. Because the backprojection requires ray tracing, in our case it is replaced with an equivalent image mapping procedure. The idea to swap the filtering and backprojection had been introduced earlier for computerized tomography (CT). Here we use this idea but develop it differently. Contrary to CT imaging, where the source and detector are rotated, in DT the subject and the flat panel detector are fixed in space. This imaging geometry allows reconstruction in planes parallel to the flat panel detector, which results in a significant simplification of the filter of backprojection algorithm. Moreover, the algorithm is not memory demanding and can be used with very large datasets. Two versions of the meshless algorithm are presented. One of them is based on convolution type filtering, while another uses filtering in the Fourier domain. Both versions are assessed and compared against the cone beam algorithm.

1. Introduction

Digital tomosynthesis (DT) is a technology that provides some of the benefits of computerized tomography (CT) but at reduced radiation dose and cost (Travish *et al* 2012, 2013, Mavalankar *et al* 2017). DT reconstructs slices within a subject from a set of projection images taken over a limited angle range. The majority of image reconstruction algorithms are common to DT and CT (Helgason 2011, Natterer 2001). The most popular ones include simultaneous algebraic reconstruction (Kak and Slaney 1988), filtered backprojection (Deans 1993), cone beam algorithm (Feldkamp *et al* 2012); and their variants. The image reconstruction can also be formulated as solving an optimization problem (Patel 2012, Klodt and Hauser 2016). All of the aforementioned methods require reconstruction volume allocation and are based on ray tracing techniques. Reconstructed three-dimensional images become available only after the entire volume is processed and the algorithm completes.

In spite of obvious similarities between CT and DT, there exist significant differences. Due to limited angle data acquisition, reconstruction in DT is performed on a slice-by-slice basis, where slices are usually taken in planes parallel to a flat panel detector. The key difference between CT and DT is that in plane (x-y) resolution in DT can be 4–10 times higher than in CT resulting in very large memory usage. In such a case it makes sense to reconstruct one slice at a time interactively instead of waiting for completion of the algorithm. This approach is especially efficient when only a part of the entire reconstruction volume is of interest.

In this paper we suggest a meshless (in the sense that no three-dimensional grid or mesh allocation is required) algorithm, which performs a user interactive, slice-by-slice reconstruction where each slice position can be chosen at runtime. This allows the display of reconstructed slices on the fly as soon as they are available. Moreover, the reconstruction slice order can be arbitrary, thus, allowing the most relevant slices to be reconstructed and displayed first. The methodology presented here is based on the filtered

backprojection algorithm adapted to DT. However, in our case the backprojection comes first and the filtering follows. Because the backprojection requires ray tracing, the backprojection in our case is replaced with an equivalent image mapping procedure.

The idea to swap the filtering and backprojection order had been introduced earlier for CT (Bates and Peters 1971, Smith *et al* 1973, Gullberg 1979) and was based on the Fourier transform. In those approaches the reconstruction procedure starts with the backprojection of attenuation images and follows with the two-dimensional forward Fourier transform, then, filtering, and, finally, the two-dimensional inverse Fourier transform (see appendix A). Here we use this idea but develop it differently. Contrary to the CT imaging, where the source and detector are rotated, in DT the subject and the flat panel detector are fixed in space. This imaging geometry allows reconstruction in planes parallel to the flat panel detector, which results in a significant simplification of the filter of the backprojection algorithm.

This paper is organized as follows: In the next section the methodology of the suggested meshless algorithm is presented. The algorithm is evaluated on experimental data sets and its results are compared to those of cone beam reconstruction. Experimental details and reconstruction results are described in the section 4. Then, we summarize and conclude. In order to make the paper self-contained appendix A outlines the traditional filter of backprojection algorithm appendix B describes the cone beam algorithm used here.

2. Methodology

Let us start with the basic facts. In order to recover desired information about internal structures, it is necessary to invert the Radon transform, that is, to solve for a function $f(\mathbf{r})$ in terms of its transform $\check{f}(p,\nu)$, where $\mathbf{r}$ is a point in three-dimensional space, ν is a unit vector perpendicular to a x-ray, and p is the (perpendicular) distance from the origin to the ray in the direction ν (see figure 1). The function $f(\mathbf{r})$ represents the spatial distribution of the transport coefficient entering the Beer–Lambert law. Then, as it is shown in the literature (Kak and Slaney 1988, Deans 1993), the function $f(\mathbf{r})$ can be recovered from $\check{f}(p,\nu)$ as:

$$f(\mathbf{r}) = \int_{|\nu|=1} d\nu \int_{-\infty}^{\infty} \check{f}(p,\nu)\, h(\nu\cdot\mathbf{r}-p)\, dp, \tag{1}$$

where h denotes the ramp filter. Introducing the notation $\xi = \nu\cdot\mathbf{r}-p$, the ramp filter in equation (1) is

$$h(\xi) = \frac{1}{2}\int_{-\infty}^{\infty} |k|^{d-1} \exp(2\pi i k\xi)\, dk, \tag{2}$$

where d stands for the space dimension. The inverse Radon transform in equation (1) is two-dimensional ($d=2$) even though it is used for the three-dimensional reconstruction.

The ramp filter, equation (2), is given by the integral whose integrand oscillates 'infinitely' quickly at both limits. On the other hand, the absolute value of a wave number k in periodic structures such as a Cartesian grid of pixels can not exceed its maximum value $k_{\max} = 1/2\lambda$, where λ denotes the pixel size (Brillouin 1953). Therefore, the infinite integration interval should be replaced with the finite one. Then, the integral equation (2) can be evaluated, which results in

$$h(\xi) = \frac{1}{4\pi^2}\left\{\pi k_{\max}\frac{\sin(2\pi k_{\max}\xi)}{\xi} - \left[\frac{\sin(\pi k_{\max}\xi)}{\xi}\right]^2\right\}. \tag{3}$$

Representing distances along coordinate axes as $\xi = \lambda n$, where $n\in\mathbb{Z}$ is the distance in pixels, and substituting the value of $k_{\max}$ into equation (3) we arrive at (Kak and Slaney 1988)

$$h(n) = k_{\max}^2\begin{cases} 1/4, & n=0,\\ -1/(\pi n)^2, & n=2\,\mathrm{m}+1, \quad m\in\mathbb{Z},\\ 0, & n=2\,\mathrm{m}, \quad m\neq 0.\end{cases} \tag{4}$$

In tomosynthesis, due to the de-magnification effect of backprojected rays, sometimes it makes sense to have the reconstructed slice resolution to be higher than that of the flat panel detector. However, in such a case the maximum value of the wave number $k_{\max}$ should be decreased to suppress high frequency artefacts. For practical purposes it should be sufficient to reduce the maximum value of the wave number by a factor of two. Then, equation (3) with $k'_{\max} = 1/4\lambda$ results in:

$$h'(n) = k'^2_{\max}\begin{cases} 1/4, & n=0,\\ (-1)^{(n-1)/2}/(\pi n) - 2/(\pi n)^2, & n=2\,\mathrm{m}+1, \quad m\in\mathbb{Z},\\ -2\left[1-(-1)^{n/2}\right]/(\pi n)^2, & n=2\,\mathrm{m}, \quad m\neq 0.\end{cases} \tag{5}$$

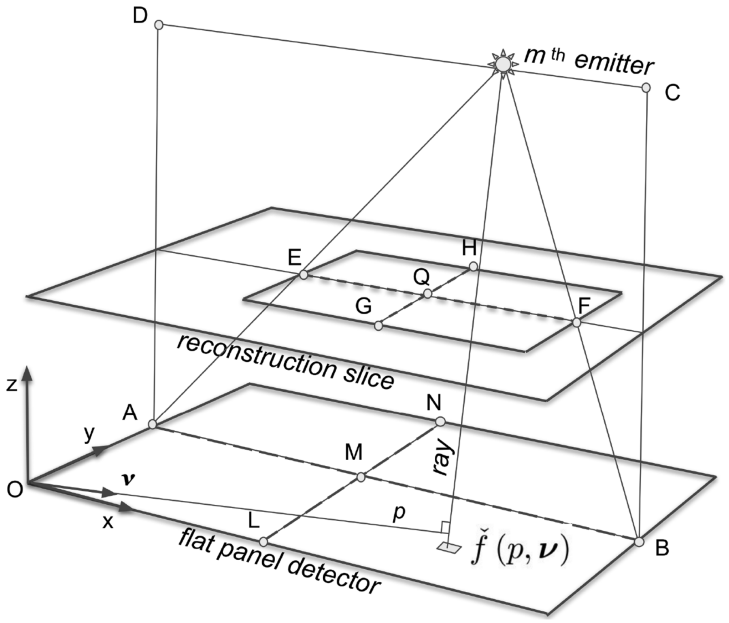

Figure 1. DT diagram.

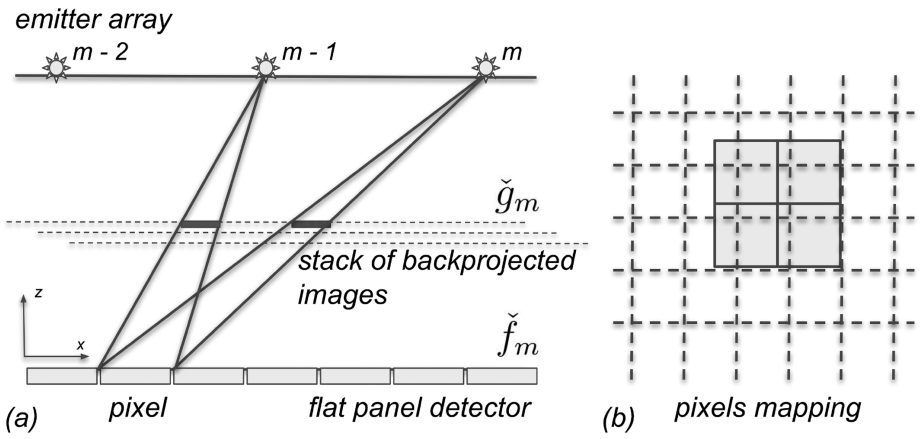

Figure 2. (a) Pixels' backprojection at the specified height along rays connecting pixel's corners to the emitter. (b) Backprojected pixels mapping onto the reconstruction slice grid.

As it is shown below, the application of the latter filter, equation (5), is effective only when the resolution of the reconstruction slice is higher than that of the flat panel detector image.

Many well-known algorithms such as cone beam reconstruction perform filtering prior to the backprojection. Here, however, we shall reverse the order and backproject first. We introduce the four-dimensional backprojection space in the same way as it is described in the literature (Levakhina 2013). The structure of the backprojection space is simple: At any particular height above a flat panel detector (assuming that the flat panel detector is placed at the bottom) a slice of the backprojection space is represented by a stack of backprojected images of $\check{f}$. Each image belongs to only one emitter. For instance, M emitters generate a stack of M images. For enumerating backprojected images we shall introduce an index (subscript) m in $\check{f}_m$, where m runs through all emitters.

Each backprojected image of $\check{f}_m$ in the stack is computed as it is shown diagrammatically in figure 2. That is, the pixel value is backprojected at the specified height along rays connecting a pixel's corners and the emitter, see figure 2(a). Then, the pixel intersection area with a backprojected image grid cell is computed, figure 2(b). This area is furthermore divided by the area of the grid cell, which results in the weighting factor. Then, the pixel value of $\check{f}_m$ is weighted by this factor and added to the value of the grid cell. This pixel mapping approach replaces a ray tracing algorithm such as the distance-driven one (De Man and Basu 2004, De Man and Fessler 2010).

Everywhere below the backprojected image of $\check{f}_m$ shall be denoted by $\check{g}_m$. As soon as the Radon transform $\check{f}_m$ has been mapped into $\check{g}_m$, the latter can be considered to be independent from the unit vector ν.

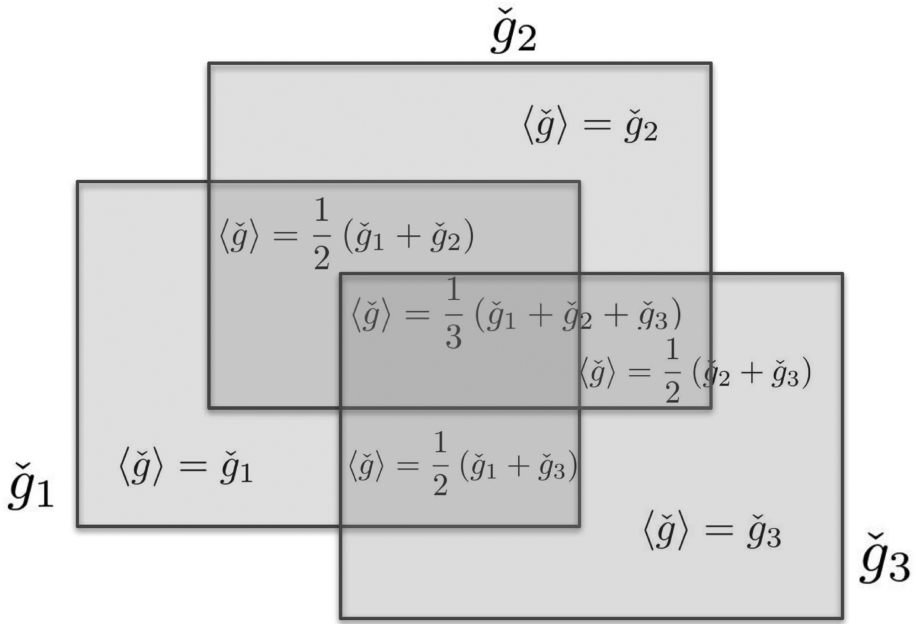

Figure 3. Backprojection space average.

Therefore, each $\check{g}_m$ is a function of local coordinates (x,y), which can be introduced for the slice of the backprojection space at any height z. Furthermore, because the convolution in equation (1) is a linear operation (in the sense that convolution of the sum of functions is the same as the sum of convolutions) we shall introduce the average:

$$\langle\check{g}(x,y)\rangle = \frac{1}{M'}\sum_{m\leq M'}\check{g}_m(x,y)\,, \tag{6}$$

where $M' \leq M$ is the number of overlapped images $\check{g}_m$ at the height z at the point (x,y), as is shown in figure 3. Then, the reconstruction formula, equation (1), can be replaced with the following:

$$\begin{aligned} f(x,y) \quad \simeq \quad & \frac{1}{2}\left\{\int_{-W}^{W} dx' h(x-x')\,\langle\check{g}(x',y)\rangle \right. \\ & \left. + \int_{-W}^{W} dy' h(y-y')\,\langle\check{g}(x,y')\rangle\right\}, \end{aligned} \tag{7}$$

where 1/2 stands for the average, and W denotes integration limits, which will be discussed later on in section 4.

Taking the average, equation (6), is crucial not only for the reason of performance but also for detector boundary artefacts reduction. Thus, when the functions $\check{g}_m$ are used in equation (7) instead of their average, due to the finite size of the flat panel detector and the limited field of view, the reconstruction slice will contain quite strong artefacts caused by the truncation of backprojected images (Zhang *et al* 2009, Sechopoulos 2013). Averaging of $\check{g}_m$ helps to alleviate this problem: The blind (truncated) areas of each $\check{g}_m$ are filled with the average of other $\check{g}_k$ $(k \neq m)$ in the stack (see figure 3).

Alternatively, reconstruction can be performed by computing the forward and inverse Fourier transforms with filtering in the Fourier domain. Let us, for the sake of brevity, denote the Fourier transform by an operator $\mathcal{F}$. Then, in a symbolic form the inversion formula reads

$$f(x,y) = \mathcal{F}^{-1}\left\{h(k)\,\mathcal{F}\,\langle\check{g}(x,y)\rangle\right\}, \tag{8}$$

where $h(k)$ denotes the ramp filter in the Fourier domain. Equation (8) is obtained from equation (1) by applying the forward and inverse Fourier transforms, where $\int\check{f}(p,\nu)\,d\nu$ is replaced with the average of backprojections $\langle\check{g}(x',y')\rangle$, Equation (6).

Strictly speaking, only the 1D forward and inverse Fourier transforms are required in equation (8) for computing the reconstruction, which can be performed, say, along the x-axis. Thus, for instance, the Fourier transform is applied along the line of intersection of the plane ABCD (see figure 1) with the reconstruction

slice, the line EF, while the line AB sweeps across the flat panel detector. However, nothing prevents us from using Fourier transforms along the y-axis as well. That is, Fourier transforms entering equation (8) become two-dimensional ones resulting in higher resolution of the reconstruction. This is the major difference between the approach suggested here and the previously proposed filter of backprojection (see appendix A) (Bates and Peters 1971, Smith *et al* 1973, Gullberg 1979). In those prior works, 2D Fourier transforms are applied over a stack of planes such as the plane ABCD, while the subject is rotated (or, completely equivalently while only the source and detector are rotated).

Formally, the forward Fourier transform of the ramp filter, equation (2), results in $|k|/2$. As it was already mentioned, the value of $|k|$ must not exceed its maximum value $\tilde{k}_{\max} = 2\pi k_{\max} = \pi/\lambda$. That is because signals (waves) with larger wave numbers can not be resolved on a grid with the pixel size λ (Brillouin 1953). Therefore, for cutting off $k > \tilde{k}_{\max}$ the ramp filter can be, for instance, a product of $|k|/2$ with the Heaviside step function $H\left(\tilde{k}_{\max} - |k|\right)$. A slightly better choice of $h(k)$ provides the product of $|k|/2$ with the Fermi–Dirac distribution:

$$h(k) = \frac{1}{2}\frac{|k|}{1 + \exp\left[\left(k^2 - \tilde{k}_{\max}^2\right)/\varepsilon\right]}, \tag{9}$$

where $\varepsilon \ll \tilde{k}_{\max}^2$ is a small number controlling the smoothness of a transition of $h(k)$ to 0 in the proximity of $\tilde{k}_{\max}$. That is, $h(k) \to \left(\frac{1}{2}\right)|k| H\left(\tilde{k}_{\max} - |k|\right)$, when $\varepsilon \to 0$. Although equation (9) has been used here, many more choices of the ramp filter can be found in the large body of literature (Oppenheim and Schafer 1975, Hamming 1977, Lyra and Ploussi 2011).

In the case of higher reconstruction slice resolution than that of the flat panel detector, the maximum value of the wave number $\tilde{k}_{\max}$ must be reduced in order to damp high frequency artefacts. In the Fourier domain this damping can be done in a more flexible way in comparison to physical space. If the pixel size of the reconstruction slice is denoted by $\lambda' \leq \lambda$, then, the corresponding maximum wave number is $\tilde{k}'_{\max} = (\lambda'/\lambda)\tilde{k}_{\max}$.

3. Regularization

It is well-known that inverse problems are typically ill-posed. DT imaging is not an exception. Contrary to CT, DT reconstructs slices from a set of projection images taken over a limited angle range. Therefore, the inverse problem suffers from incompleteness of data. This incompleteness manifests itself in the appearance of negative numbers (especially in regions where the transport coefficient should be 0), and poor image quality. To address this issue, the problem must be regularized.

In the case of equation (7), a finite convolution window W has a regularization effect. This follows from the fact that the ramp filter integrates to 0. Truncation of the integration path results in a positive value of the integral. That is, an application of the truncated filter lifts negative values up. Moreover, the finite convolution window size not only improves the reconstruction quality but also appreciably reduces computational load. Moreover, the tails of the ramp filter decay fast enough making convolution over the entire interval unnecessarily. The same regularization effect has a beneficial addition of a small number $\alpha \ll 1$ to the diagonal of the ramp filter, i.e. to the values with $n = 0$ in equations (4) and (5).

Similarly, in the Fourier domain an addition of a small number to $|k|$ in equation (9) has a regularization effect. That is equation (9) becomes

$$h_\alpha(k) = \frac{1}{2}\frac{|k| + \alpha\Delta k}{1 + \exp\left[\left(k^2 - \tilde{k}_{\max}^2\right)/\varepsilon\right]}, \tag{10}$$

where $\alpha \ll 1$ is the regularization parameter, and Δk denotes the size of the reciprocal lattice cell. A typical value of α is about 0.01 in our case.

4. Results

The presented algorithm has been assessed on experimental data. To simulate an array of emitters, a single x-ray source was moved on a mechanical stage through 45 positions (a regular 7×7 grid with the corners missing with positions separated by 10 mm). The source was a Newton Scientific M237 monoblock operated at 60 kV and 50 μA for 100 ms in each position on the grid with each cone having a full opening angle of 110 °. The Source to Image Distance (SID) between the focal spot and detector was set to 120 mm. The

Figure 4. Antique wrist joint bones.

detector used was a Teledyne Shad-o-Box 3 K HS with 50 μm pixels covering an area of 114 $\times$ 64 mm. Attenuation images were computed as $\ln(I_0/I)$, where I_0 is the recorded empty space intensity, and I is the attenuated intensity due to x-ray absorption by an object.

Antique wrist joint bones had been chosen as the first phantom for the algorithm evaluation. They were placed directly on the flat-panel detector and imaged, as shown in figure 4. The internal structure of the bones is reconstructed by employing the cone beam algorithm (see appendix B) and two versions of the meshless approach. The former is used for comparison reasons. The first version of the meshless approach employs the convolution type of the ramp filter, while the second one performs filtering in the Fourier domain. Reconstructed slices are displayed in figure 5.

The first row shows slices at different heights computed with the cone beam algorithm. The second and the third rows present reconstruction slices with the meshless approach with the convolution and Fourier type filtering, correspondingly. Each column shows slices at a specified height, which value is displayed at the top left corner. The image histogram is shown below each image. Because image intensity counts have a very wide dynamic range, counts are expressed in decibels (dB). The image intensity is given in arbitrary units along the abscissa axis (this is because original images are 16-bit and its intensity is converted to double precision real numbers and scaled down prior to the reconstruction).

As it is seen in figure 5, the reconstruction quality differs. Image quality can be evaluated by using various measures. The most common one is the signal to noise ratio: $SNR = \bar{I}/\sigma$, where the $\bar{I}$ denotes the image mean intensity, and σ is standard deviation of the image intensity. Computation of this quantity requires a free from noise reference image. Clearly, there is no such image in our case. Despite that, the reconstructed image can be denoised and used as a reference one. The most straightforward way of denoising is the application of the Gaussian filter. The edge preserving Perona-Malik anisotropic diffusion technique could be a better alternative to it (Perona and Malik 1990). Another way of noise removal is the filtering in the Fourier domain, thus, truncating wave numbers at the value $k = k_{\max}/2$. All three techniques provide similar results. A corresponding number of iterations for the Perona-Malik approach can be estimated according to a 7 by 7 pixels Gaussian window size or so by using the Courant-Friedrichs-Lewy stability condition. The same value of the image standard deviation σ allows for computation of the contrast-to-noise ratio, which is defined as $CNR = \bar{I}_{\max}/\sigma$, where $\bar{I}_{\max}$ stands for the maximum image intensity averaged over a small window. Another useful measure is the Weber contrast $C = (\bar{I}_{\max} - I_B)/I_B$, where I_B is the image background intensity, and the image feature has been chosen as $\bar{I}_{\max}$. In the region of interest (ROI) the most likely (or the most probable) value of the image intensity may serve as the background intensity I_B. This value is more or less the same for images produced by all three methods. ROI has been chosen as a part of the reconstructed image corresponding to the maximum number of overlapping backprojected attenuation images, thus, excluding regions with possible detector boundary artefacts.

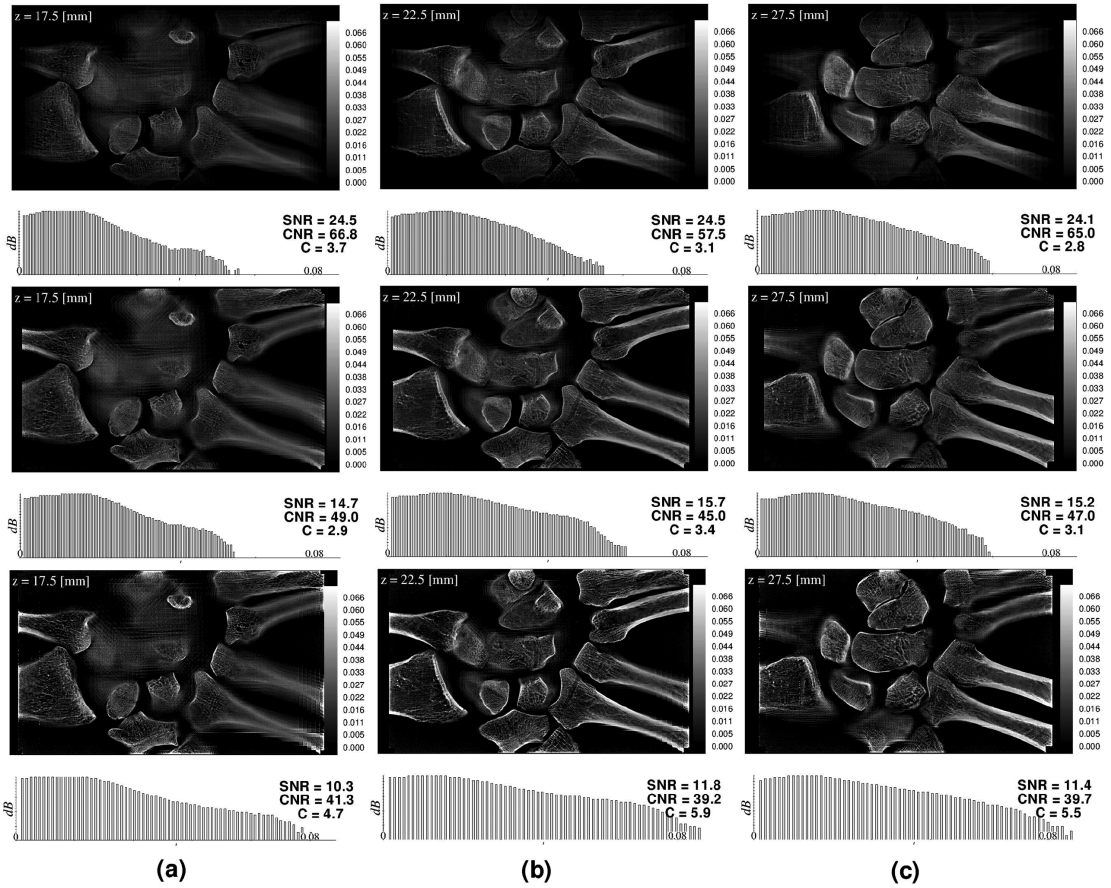

Figure 5. Reconstructed slices of the antique wrist joint. The first row shows results of the cone beam algorithm. The second and third rows present results of the meshless approach with the convolution and Fourier type flittering, respectively. Column (a) displays reconstructed slices by three methods at the height 17.5 mm above the flat panel detector, (b) 22.5 mm, and (c) 27.5 mm. Images are presented in the same grey range for comparison. Image histograms are shown below each image. They display counts in decibels (dB) along the ordinate axis. The image intensity is given in arbitrary units along the abscissa axis.

Thus, according to histograms the meshless method with filtering in the Fourier domain provides the highest contrast. Weber contrast indicates this as well. Its average over three slices shown in the last row in figure 5 is about 5.4. Weber contrasts for the cone beam algorithm and the meshless approach with convolution type filterring are roughly the same, which are 3.2 and 3.1, respectively. On the other hand, the noise level for the meshless technique is higher, which is indicated by both SNR and CNR.

A fox's jaw was chosen as the second phantom. It might present some interest for application of tomosynthesis in dental imaging. The SID here was increased to 185 mm. The subject is shown in figure 6. As in the first case the reconstruction was computed by a cone beam algorithm and two versions of the meshless method. Reconstruction results are shown in figure 7. Image histograms are placed below each image. By comparing histograms, it is seen that the reconstruction contrast is noticeably higher for the meshless method. Weber contrast tells the same. Because SNR is lower for both versions of the meshless approach than that of the cone beam algorithm, the noise level is higher. That is, higher contrast comes with the higher level of noise as expected.

Although the filtering in the Fourier domain gives higher overall contrast than the convolution type of filtering, it suffers from the detector boundary artefacts problem. Figure 8 illustrates this issue, where the out of focus region at the bottom right coner of the antique wrist joint bones is magnified for this purpose. Thus, while the reduction of detector boundary artefacts is manageable for the convolution type filtering, currently it is not clear how to avoid these artefacts in the Fourier domain. This problem can be especially severe when reconstruction slices are computed far above the flat panel detector. Regarding this issue, the convolution type filtering is preferable over the Fourier domain filtering until a solution to this issue is found.

The algorithmic efficiency of the Fourier approach is usually higher than that of the convolution one. However, in our case the difference is not that significant for the following reasons: Firstly, as was mentioned above, a finite convolution window size is used for regularization purposes. Secondly, a fast Fourier transform is most efficient for power-of-two vector (array) sizes. That is, for a high resolution flat panel detector allocated vectors can be much larger than the actual detector size. Thus, for instance, the Teledyne

Figure 6. Fox's jaw phantom.

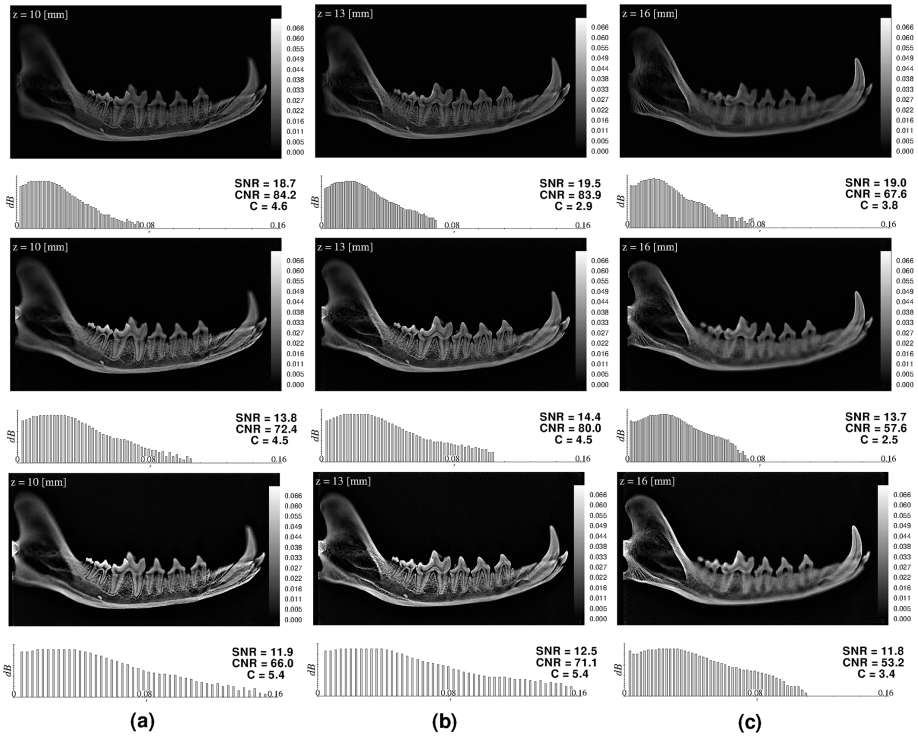

Figure 7. Reconstructed slices of the fox's jaw. The first row demonstrates the cone beam algorithm. The meshless approach with both type filtering is shown in the second and the third rows. Columns (a), (b) and (c) correspond to different slice heights above the flat panel detector. Image histograms are shown below each reconstruction slice.

Shad-o-Box detector has dimensions of 2304 by 1300 pixels, which requires vector sizes of 4096 and 2048 pixels, respectively. Note that these pixel counts (about 3 million) are significantly higher than in CT (~0.3 million). Moreover, the Fourier transform involves computations with complex numbers, which are represented by two real ones, and therefore doubles the required vector sizes. In addition, the forward and inverse Fourier transforms are used twice. Overall, in our implementation, the Fourier approach is about 1.2 times faster than the convolution type filtering, when the convolution window is set to $W = 350$ pixels from

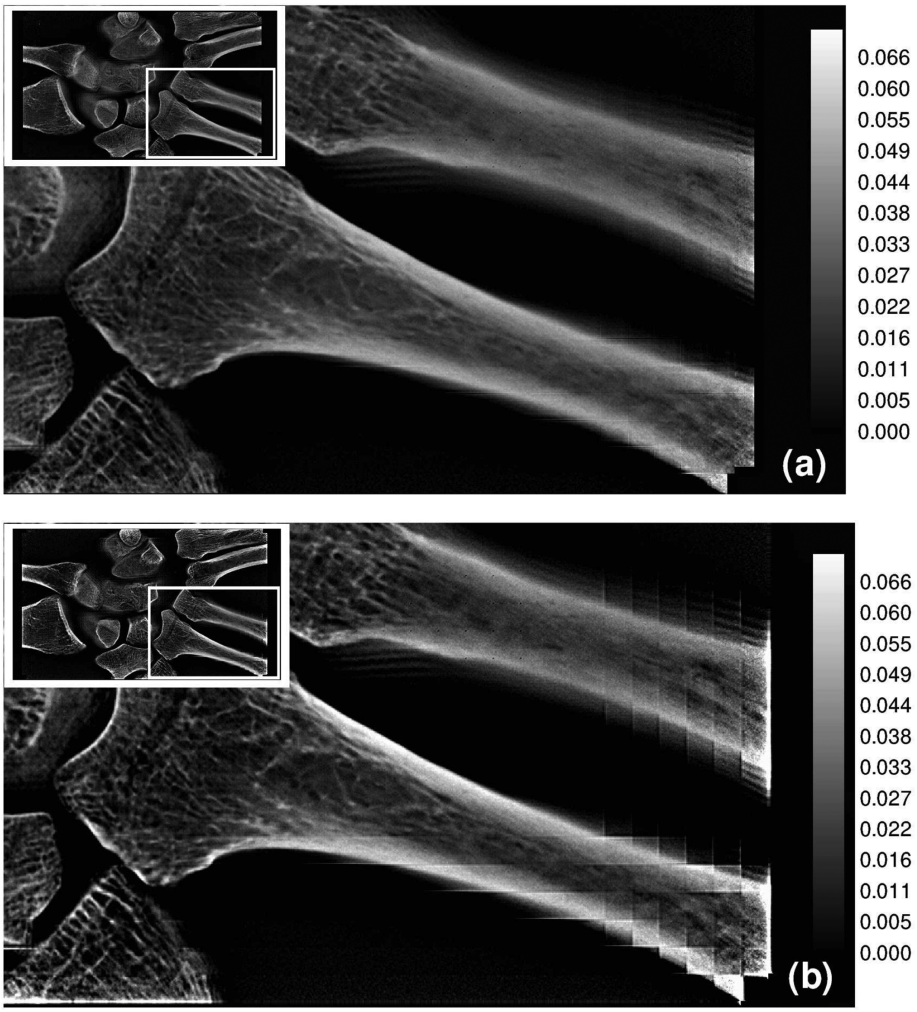

Figure 8. Flat panel detector boundary artefacts. (a) Convolution type filtering. (b) Filtering in the Fourier domain.

the left and right of the current pixel. This is very close to the theoretical estimate: $4WN_c/4N_f\log_2(N_f) \simeq 1.25$, where N_c and N_f are corresponding vector sizes. With a larger detector size, the convolution type filtering can even be faster than the Fourier approach unless the detector size in pixels is exactly a power of two.

The computational efficiency of the cone beam algorithm depends on the number of reconstructed slices. For only a few slices, say 10, the computational efficiency per slice is comparable with the meshless approach with the convolution type filtering (assuming the same window size W). However when the number of slices increases, the computational efficiency per slice of the cone beam improves. Thus, for 100 slices the cone beam algorithm is about $1.4 - 1.6$ times faster than the meshless approach. This is an expected result because in our version of the cone beam algorithm only one convolution per pixel across the flat panel detector has been used. On the other hand, in contrast to the meshless approach, the cone beam algorithm requires additional allocation of a three-dimensional grid, which for the case of 100 slices takes approximately 2.4 gigabytes when real numbers are represented with double precision in comparison to just one slice storing the average of backprojections.

Finally, we discuss the choice of the ramp filter. Due to the de-magnification effect, when pixel values are backprojected toward the reconstruction volume, super-resolution can be observed (Acciavatti and Maidmenta 2012). In order to fully capture the phenomenon, the reconstruction slice resolution should be higher than that of a flat panel detector. However, in this case the value of the maximum wave number $k_{\max}$ is dictated by the pixel size of the flat panel detector. Othewise, the reconstruction will suffer from high frequency artefacts.

For illustration of the filter choice, a 1.5–20 lp/mm Line pair phantom (Type 39-003, Leeds Test Objects, Boroughbridge, UK) has been imaged. The reconstruction slice resolution is increased to twice the resolution of the flat panel detector. Reconstuction results are shown in figures 9 and 10, where figure 9 presents a slice computed with the convolution type filtering, while figure 10 displays the results of the Fourier domain filtering. Images are zoomed for visualization purposes.

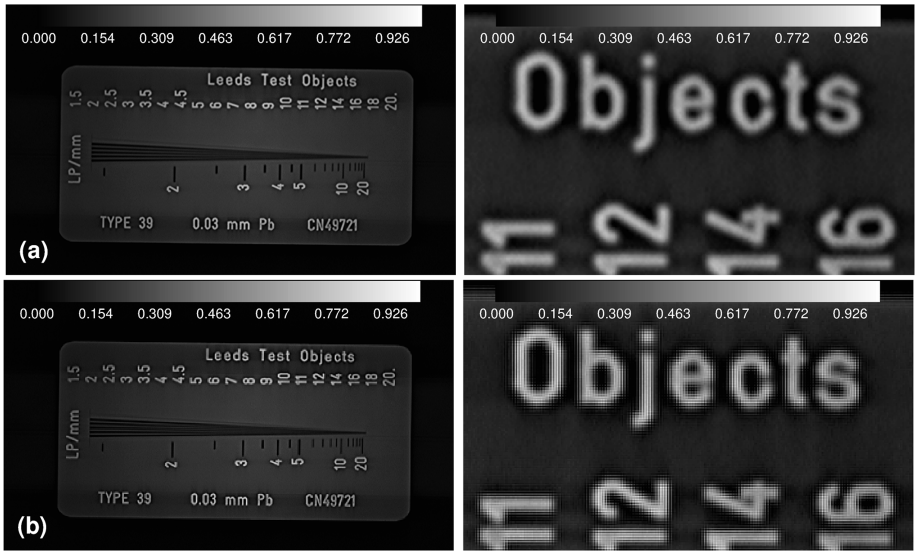

Figure 9. 1.5–20 lp/mm Line pair phantom reconstructed with the convolution type of filtering: (a) Optimal choice of $k'_{\max} = 1/4\lambda'$, where λ' denotes the slice pixel size. (b) $k'_{\max} = 1/2\lambda'$ is too large so there are high-frequency artefacts.

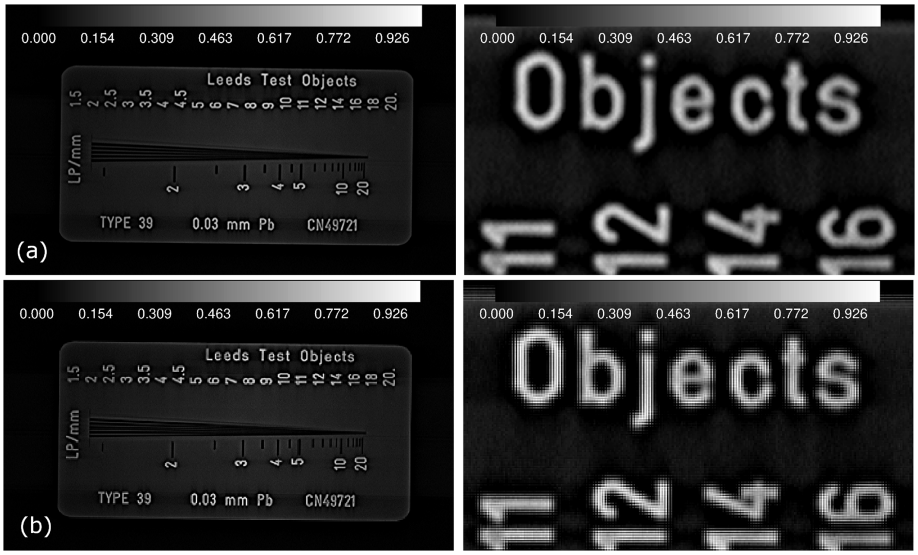

Figure 10. 1.5–20 lp/mm Line pair phantom reconstructed with filtering in the Fourier domain: (a) Optimal choice of $\tilde{k}'_{\max} = \pi/2\lambda'$, where λ' denotes the slice pixel size. (b) $\tilde{k}'_{\max} = \pi/\lambda'$ is too large so there are high frequency artefacts.

Thus, figure 9(a) presents results when equation (5) has been applied. Further zoomed part of the phantom is shown on the right. On the other hand, figure 9(b) displays reconstruction results computed with the ramp filter given by equation (4). Zoomed part on the right clearly illustrates high frequency artefacts, which are absent in figure 9(a). Because the Fourier type of filtering exhibits higher contrast, these high frequency artefacts are more profound in figure 10(b) where $\tilde{k}_{\max}$ is chosen. Results with $\tilde{k}'_{\max} = (1/2)\,\tilde{k}_{\max}$ are shown in figure 10(a) and present reasonable good quality.

5. Summary and conclusions

A novel meshless reconstruction algorithm is presented and assessed on experimental data. Its reconstruction quality is compared against cone beam reconstruction. The meshless approach has several advantages. Firstly, particular reconstruction slices can be chosen at runtime, and, therefore, this approach constitutes a user interactive reconstruction technique in contrast to the majority of well-known algorithms. This allows the display of reconstructed slices on the fly as soon as they are available. Moreover, the reconstruction slice order can be arbitrary, thus, allowing the most relevant slices to be reconstructed and displayed first. Secondly, for thick objects, it is able to produce slices of higher contrast than many techniques such as the

cone beam one. Thirdly, it is fast and not memory demanding. Thus, in comparison to the cone beam algorithm, which is considered as one of the most efficient algorithms, the meshless approach requires less memory.

Acknowledgments

This work was partially supported by InnovateUK grant 133590.

Appendix A. Filter of backprojections

The traditional filter of backprojection algorithm is briefly outlined here. The reconstruction procedure starts with the backprojection of attenuation images and follows with the two-dimensional forward Fourier transform, then, filtering, and, finally, the two-dimensional inverse Fourier transform. Originally, this reconstruction technique had been developed for parallel rays imaging (Bates and Peters 1971, Smith *et al* 1973) and extended later for the fan-beam data (Gullberg 1979).

The three-dimensional distribution of the transport coefficient $f(x,y,z)$ is reconstructed on a slice-by-slice basis along, say, the z -axis, which is chosen as the subject rotation axis here. That is, the three-dimensional reconstruction is performed as a stack of two-dimensional (x,y)-slices. Images are acquired on planes parallel to the z -axis as it is shown in figure A1.

In order to explain the technique, let us start with the backprojection operator $\mathcal{B}$ first, which is introduced as

$$b(x,y) = \mathcal{B}\check{f}(p,\nu)\,, \tag{A1}$$

where $\check{f}$ denotes the Radon transform of $f(x,y)$ is a point in the slice lying perpendicular to the z-axis; ν is the 2D unit vector perpendicular to x-ray; and p is the (perpendicular) distance form the origin to the ray in the direction ν. It is known (Deans 1993), that the true image $f(x,y)$ convolved with $1/r$, where

$$r = \left[(x-x')^2 + (y-y')^2\right]^{1/2}, \tag{A2}$$

yields the backprojection image

$$b(x,y) = \iint_{-\infty}^{\infty} \frac{f(x',y')}{r}\,dx'dy'. \tag{A3}$$

Applying the 2D Fourier transform to $b(x,y)$, equation (A3), we arrive at

$$\tilde{b}(\mathbf{k}) = \mathcal{F}_2 b(x,y) = |\mathbf{k}|^{-1}\tilde{f}(\mathbf{k})\,, \tag{A4}$$

where $\tilde{f}(\mathbf{k})$ denotes the 2D Fourier transform of $f(x,y)$, and $\mathbf{k} = \left(k_x, k_y\right)^T$. Combining all these formulas above we obtain the following

$$\tilde{f}(\mathbf{k}) = |\mathbf{k}|\,\tilde{b}(\mathbf{k}) = |\mathbf{k}|\,\mathcal{F}_2 b(x,y) = |\mathbf{k}|\,\mathcal{F}_2\mathcal{B}\check{f}. \tag{A5}$$

The inverse Fourier transform, $\mathcal{F}_2^{-1}$, of both sides yields

$$f(x,y) = \mathcal{F}_2^{-1}\left[|\mathbf{k}|\,\mathcal{F}_2\mathcal{B}\check{f}\right]. \tag{A6}$$

Therefore, algorithmically, we have to perform series of operations:

$$\check{f} \to b \to \tilde{b} \to \tilde{f} \to f. \tag{A7}$$

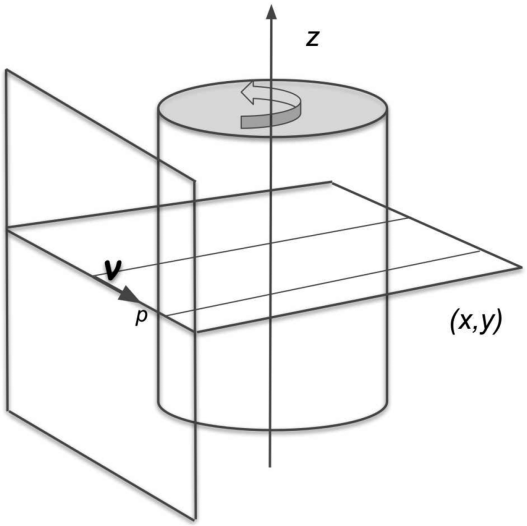

Figure A1. Filter of backprojection imaging diagram.

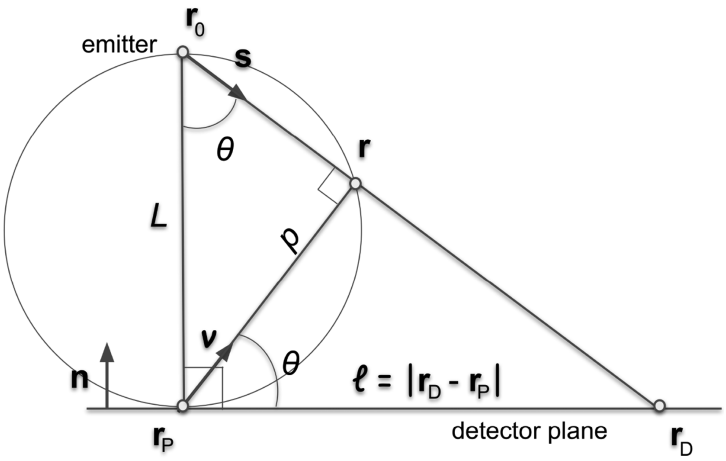

Figure B2. Fan plane geometry. Parameter p parameterizes a circle. The stereographic projection maps this circle onto a line across the detector plane.

Appendix B. Cone beam algorithm

The version of the cone beam algorithm which is used in this paper is based on the exact Radon inversion formula (Deans 1993). It reads:

$$f(\mathbf{r}) = \frac{1}{4\pi^2}\int_{|\nu|=1} d\nu \fint_{-L}^{L} \frac{\partial \check{f}(p,\nu)}{\partial p}\frac{dp}{t-p}, \tag{B8}$$

where $t = \nu \cdot \mathbf{r}$, and the integral over p is understood to be the Cauchy Principal Value, which is indicated by a dash. Note that in our case of cone projection, the integration is performed over the interval $[-L, L]$. This is because the distance parameter p parameterizes a circle in three-dimensional space, as it is shown in figure B2. Next, the integration contour is mapped onto the line across the image plane by applying the stereographic projection:

$$\ell = pL\left(L^2 - p^2\right)^{-1/2}, \quad p = \ell L\left(L^2 + \ell^2\right)^{-1/2}. \tag{B9}$$

This results in:

$$f(\mathbf{r}) = \frac{1}{4\pi^2 L}\int_{|\mathbf{s}|=1} R(\ell_0)\, d\mathbf{s} \fint_{-\infty}^{\infty} \frac{\partial \check{f}(\ell,\varphi)}{\partial \ell}\frac{d\ell}{\ell_0 - \alpha(\ell)\,\ell}, \tag{B10}$$

where $R(\ell_0) = \left(L^2 + \ell_0^2\right)^{1/2}$ is the path length of a ray hitting the current pixel; $\ell_0 = tL\left(L^2 - t^2\right)^{-1/2}$ is the distance from the local origin on the flat panel detector to the current pixel; ℓ is the distance parameter across the flat panel detector; **s** is the unit vector along the ray; φ is the azimuthal angle in the plane of the flat panel detector which defines the integration path; and the weighting factor $\alpha(\ell)$ is given by

$$\alpha(\ell) = \left(\frac{L^2 + \ell_0^2}{L^2 + \ell^2}\right)^{\frac{1}{2}}. \tag{B11}$$

The inversion formula for a parallel ray projection is recovered from equation (B10) by letting $L \to \infty$, as it should.

Siddon's algorithm (Siddon 1985, Jacobs *et al* 1998) has been applied for ray tracing across the flat panel detector for computing the integration path in equation (B10). That is, a line across an image is represented by two rays fired in opposite directions starting from the pixel with polar coordinates (ℓ_0, φ), see equation (B10). Due to the Cauchy Principal Value integral over ℓ, the choice of starting integration point inside the pixel is important. Denoting indices of the pixel at (ℓ_0, φ) by i and j, the Cartesian coordinates of the starting integration point must be at the center of the pixel, i.e. $([i + 1/2]\,\Delta x, [\,j + 1/2]\,\Delta y)$. This choice provides that line segments of both rays are of the same lengths, while line segments at the pixel where the convolution is computed are omitted. When the convolution is computed, the pixel value at (ℓ_0, φ) is backprojected toward the reconstruction volume by employing the distance-driven tay tracing algorithm (De Man and Basu 2004, De Man and Fessler 2010).

References

Acciavatti R J and Maidmenta A D A 2012 Observation of super-resolution in digital breast tomosynthesis *Med. Phys* **39** 7518–39

Bates R H T and Peters T M 1971 Towards improvements in tomography *N. Z. J. Sci* **14** 883–96

Brillouin L 1953 *Wave Propagation in Periodic Structures* (New York: Dover)

De Man B and Basu S 2004 Distance-driven projection and backprojection in three dimensions *Phys. Med. Biol* **49** 2463–75

De Man B and Fessler J A 2010 Statistical iterative reconstruction for x-ray computed tomography *Biomedical Mathematics: Promising Directions in Imaging, Therapy Planning and Inverse Problems* ed Y Censor, M Jiang and G Wang (Madison, WI: Medical Physics Publishing) pp113–40

Deans S R 1993 *The Radon Transform and Some of its Applications* (New York: Dover)

Feldkamp L A, Davis L C and Kress J W 1984 Practical cone-beam algorithm *J. Opt. Soc. Am.* A **1** 612–9

Gullberg G T 1979 The reconstruction of fan-beam data by filtering the back-projection *Comput. Graph. Image Proc* **10** 30–47

Hamming R W 1977 *Digital Filters* (Englewood Cliffs, NJ: Prentice-Hall)

Helgason S 2011 *Integral Geometry and Radon Transforms* (Berlin: Springer)

Jacobs F, Sundermann E, De Sutter B, Christiaens M and Lemahieu I 1998 A fast algorithm to calculate the exact radiological path through a pixel or voxel space *J. Comput. Inf. Technol* **6** 89–94

Kak A C and Slaney M 1988 *Principles of Computerized Tomographic Imaging* (Piscataway, NJ: IEEE)

Klodt M and Hauser R 2016 3D image reconstruction from X-Ray measurements with overlap (arXiv: 161107390)

Levakhina Y 2013 Three-dimensional digital tomosynthesis *PhD Thesis* University of Lübeck

Lyra M and Ploussi A 2011 Filtering in SPECT Image Reconstruction *Int. J. Biomed. Imaging* **2011** 693795

Mavalankar A, Cameron J and Travish G 2017 Operating high-current field emitters in a commercial X-ray source *2017 30th Int. Vacuum Conf. (IVNC)* (https://doi.org/10.1109/IVNC.2017.8051654)

Natterer F 2001 *The Mathematics of Computerized Tomography* (Philadelphia, PA: SIAM)

Oppenheim A V and Schafer R W 1975 *Digital Signal Processing* (Englewood Cliffs, NJ: Prentice-Hall)

Patel K 2012 Imaging with X-Ray emitter arrays *MS Thesis* University of Oxford

Perona P and Malik J 1990 Scale-space and edge detection using anisotropic diffusion *IEEE Trans. Pattern Anal. Mach. Intell* **12** 629–39

Sechopoulos I 2013 A review of breast tomosynthesis. Part II. Image reconstruction, processing and analysis and advanced applications *Med. Phys* **40** 014302

Siddon R L 1985 Fast calculation of the exact radiological path for a three-dimensional CT array *Med. Phys* **12** 252–5

Smith P R, Peters T M and Bates R H T 1973 Image reconstruction from finite numbers of projections *J. Phys A: Math. Nucl. Gen* **6** 361–82

Travish G, Rangel F J, Evans M A, Hollister B and Schmiedehausen K 2012 Addressable flat-panel x-ray sources for medical, security and industrial applications *Proc. SPIE* **8502** 85020L

Travish G, Rangel F J, Evans M A, Hollister B and Schmiedehausen K 2013 Applying high frame-rate digital radiography and dual-energy distributed-sources for advanced tomosynthesis *Proc. SPIE* **8853** 88530H

Zhang Y, Chan H-P, Sahiner B, Wei J, Ge J, Zhou C and Hadjiiski L M 2009 Artifact reduction methods for truncated projections in iterative breast tomosynthesis reconstruction *J. Comput. Assist. Tomogr* **33** 426–35